

Comprehensive description of color centers by wave function theory: a CASSCF-NEVPT2 study of the NV defect in diamond

Zsolt Benedek,^{1,2} Ádám Ganyecz,^{1,2} Anton Pershin,^{1,3} Viktor Ivády,^{2,4,5,*} and Gergely Barcza^{1,2,†}

¹*HUN-REN Wigner Research Centre for Physics, H-1525, Budapest, Hungary*

²*MTA-ELTE Lendület "Momentum" NewQubit Research Group,*

Pázmány Péter sétány 1/A, 1117 Budapest, Hungary

³*Department of Atomic Physics, Institute of Physics,*

Budapest University of Technology and Economics,

Műegyetem rakpart 3., H-1111 Budapest, Hungary

⁴*Department of Physics of Complex Systems, Eötvös Loránd University, Egyetem tér 1-3, H-1053 Budapest, Hungary*

⁵*Department of Physics, Chemistry and Biology,*

Linköping University, SE-581 83 Linköping, Sweden

(Dated: June 10, 2024)

Paramagnetic point defects in wide-bandgap semiconductors, characterized by atomic-like in-gap defect states, constitute a unique challenge for ab initio modeling. In this theoretical study, we aim to devise a wave-function only computational protocol, exemplified on the prominent nitrogen-vacancy (NV) center in diamond, which enables the full characterization of future quantum bit candidates implemented in color centers. We propose the application of the second order n -electron valence state perturbation theory on top of the complete active space self-consistent field approximation (CASSCF-NEVPT2) to provide a balanced ab initio level description of the correlation effects yielded from the defect orbitals and the embedding nanodiamond. By relaxing the molecular cluster under the compression of the surrounding bulk material, we manage to model both the vertical and relaxed experimental electronic spectra within an average error margin of 0.1 eV. Furthermore, the experimentally observed Jahn-Teller behavior of 3E and 1E states, the measured fine structure of the triplet electronic states, as well as the expected spin-selectivity are quantitatively reproduced by the presented methodology. Our findings showcase that using conventional wavefunction-based quantum chemical approaches on carefully crafted cluster models can be a competing alternative for discussing the energetics of point defects in solids.

I. INTRODUCTION

Owing to their unique magneto-optical properties, point-like defects in crystals that act as individual color centers have risen to fame with the advance of quantum technologies. In the last decade, such solid-state color centers have been applied as high-resolution nano-sized sensors^{1,2} thanks to their sensitivity to external electromagnetic fields, strain, and temperature. Furthermore, a large variety of single-photon emitters³⁻⁵ has been identified in defected solids by now, which is an integral component in quantum computation⁶ and quantum secure communication⁷. Moreover, paramagnetic defects that enable spin-selective decay pathways could be used to create quantum bits^{8,9}, controllable through the optically detected magnetic resonance (ODMR) technique¹⁰.

From a theoretical point of view, point defects hosted in wide-bandgap semiconductors behave like atoms featuring localized defect states in a screening medium of the bulk electrons. Spin-qubit applications relying on ODMR processes necessitate a complete understanding of the magneto-optical properties of the defect centers where strongly correlated singlet many-body states can play a vital role¹¹. Therefore, the proper models of these color centers require simultaneous high-level treatment of both static and dynamic correlation effects corresponding to the localized defect and the embedding solid respectively¹²⁻¹⁴.

In the first place, the numerical exploration of the crystalline structures with point defect⁵ is typically performed using density functional theory (DFT) based methods¹⁵. This approach enables the computation of many relevant properties of color centers, such as formation energies, charge transition levels, spin states, hyperfine tensors, zero phonon lines, and photoluminescence spectra, albeit with varying accuracy, as summarized in reviews Ref. 5, 11, 16, and 17. However, the widely applied DFT is an inherently single-determinant method for ground state calculations, and it has limitations in describing states of strongly multireference nature.^{18,19} Thus, despite the tremendous theoretical progress in recent decades in studying correlated electronic states with DFT²⁰, the quantitative description of solid state color centers still poses challenges^{21,22}.

To further improve the theoretical description of spin-active defects, there is a strong need for the development of a universally applicable wave function theory (WFT) based protocol that can accurately handle multiconfigurational problems. In fact, the defect community has already begun exploring post-DFT and post-Hartree-Fock methods for this purpose. Without attempting to provide an exhaustive list, we mention several common methods, including time-dependent DFT²³⁻²⁶, variational DFT²⁷, complete active space self-consistent field (CASSCF)^{28,29}, multireference configuration interaction²⁸, Monte Carlo configuration inter-

action³⁰, configuration interaction constrained random phase approximation³¹, density matrix renormalization group approach³², equation of motion coupled cluster theory³³, GW based approximations^{34,35}, and various quantum embedding theories^{12,14,36–39}. These methods have mainly been benchmarked on the negatively charged nitrogen-vacancy (NV⁻) center in diamond, which is the most relevant and extensively studied optically active spin defect to date¹¹. While the distinct models concluded a largely consistent overall picture of the NV⁻ vertical electronic structure, there has been less satisfactory quantitative agreement with the experimental data in most cases. Furthermore, the proper description of magneto-optical properties, taking into account geometry relaxation effects, that are important for a detailed understanding of a defect center, has not been fully addressed within high-level WFT approaches.

In this work, we take a step in this direction by presenting a novel computational strategy based entirely on conventional quantum chemical wavefunction approaches. First, we highlight the critical importance of properly representing the hosting crystalline solid within minimal models of diamond clusters passivated by hydrogen atoms. By applying the CASSCF approach on the defect orbitals, we demonstrate that the geometry relaxation only affects the immediate surroundings of the point defect. The corresponding CASSCF electronic structure was found to be improved by the NEVPT2 perturbative energy correction, which incorporates the dynamic correlation effects of the embedding environment. We demonstrate the potential of this methodology by a comprehensive modeling of the prototypical color center, NV⁻ in diamond, aligning closely with the most firmly established experimental observations in the research field.

The rest of our paper is organized as follows. In Sec. II., we briefly present the theoretical background of the applied ab initio methods for interested readers, while the actual details of our performed computations are given in Sec. III. In Sec. IV, the construction of the cluster models for the NV⁻ defect center in cubic diamond crystal is presented. Sec. V discusses our numerical results comparing them to the experimental predictions. Finally, we conclude on the practical applicability of the presented WFT calculations in Sec. VI.

II. AB INITIO METHODS

Our computational approach integrates the CASSCF and NEVPT2 methods to account for both static and dynamic correlation effects on the electronic structure. In the following, we briefly summarize the features of the applied approaches, highlighting the potential advantages of the CASSCF-NEVPT2 method for studying color centers with highly correlated electronic states arising from the atomic-like defect orbitals.

A. Static correlation (CASSCF)

The complete active space self-consistent field (CASSCF) method^{40–42} captures the full range of correlation effects within a specific set (“active space”) of molecular orbitals (MOs). During the CASSCF calculations, a two-step cycle of the full configuration interaction (FCI) solution and orbital optimization (i.e. mixing active and external orbitals to minimize the energy) is repeated until reaching convergence.

Thus this method is capable of providing a practically exact solution in case all orbitals with non-negligible correlation effects are included in the active space. Unfortunately, owing to the exponential scaling of the approach with respect to the number of active orbitals, only a handful of orbitals (up to 20) can be set to active without further approximations. The remaining orbitals are kept frozen on the Hartree–Fock level during the solution of the configuration interaction problem, and only influence the correlation energy through some orbital mixing during the orbital optimization procedure.

Note that the CASSCF approach is suitable for studying not only the ground state, but also the many-body excitations, where the orbitals are optimized either for an ensemble of target states in a state-averaged manner (SA-CASSCF), or for one selected state in a state-specific manner (SS-CASSCF). The latter approach is also suitable for geometry relaxation of excited electronic states.

Overall, the method provides a highly accurate description of the static correlation (i.e. the mixing of electronic states of different orbital occupation patterns) but it fails to assess dynamic correlation effect of the frozen inactive (doubly occupied) and virtual (unoccupied) orbitals. The resulting CASSCF wave function is qualitatively correct, and it can be used for geometry optimization and vibrational analysis. However, neglecting the dynamic correlation generally results in dramatic errors in energy differences (gaps) between different electronic states.

In computational chemistry⁴³, the proper choice of the active space is not always straightforward. Nevertheless, point defects in crystals typically yield a few of so-called defect orbitals, which define a chemically intuitive CAS. Note that these defect-localized MOs lie inside a large (> 2 eV) band gap shaping the low-energy excitations. In the case of the NV center in diamond⁴⁴, four relevant defect orbitals can be identified, specifically those that originate from the dangling bonds of the three carbons and a nitrogen adjacent to the vacancy.

B. Dynamic correlation (NEVPT2)

While pristine diamond is known for its lattice structure formed by single covalent bonds, it is essential to take into account dynamic correlation to reproduce experimental data^{45–47}. Accordingly, handling the correlation effects of the crystalline hosting the point-defect,

which are completely omitted by the CASSCF approach, is critical.

In the literature, various concepts have been developed to provide an *a posteriori* correction to the CASSCF solution. Building on our previous work on point defects in hexagonal boron-nitride layers^{48,49}, we employ the second-order n -electron valence state perturbation theory (NEVPT2)⁵⁰⁻⁵². This method, a type of multireference perturbative approach, can be thought of as an extension of the second-order Møller-Plesset perturbation theory⁵³ to multireference systems. Owing to the construction of the zero-order Dyll Hamiltonian⁵⁴ and to the choice of perturbers, the NEVPT2 can provide a size-consistent theory on top of the CASSCF reference, that is free of intruder states and spin-contamination issues.

To speed up the NEVPT2 calculations by using only a limited selection of perturbers, various contraction schemes were formulated that carefully balance accuracy with practicality.⁵⁰ Recent technical developments, such as the application of the cumulant approximation⁵⁵, pre-screening⁵⁶, resolution of identity and domain-based local pair natural orbitals⁵⁷, have enabled the routine treatment of molecular systems with thousands of orbitals.

By now, in case of sizeable active spaces, the computational bottleneck of the CASSCF-NEVPT2 procedure may often no longer be attributed to the NEVPT2 energy correction itself, but rather to the preceding CASSCF calculation which scales exponentially with respect to the number of active orbitals.⁵⁸

C. Fine structure and spin properties

The splitting of the triplet electronic states induced by secondary magnetic effects, which is neglected by the non-relativistic CASSCF solution, can also be estimated *a posteriori* by quasi-degenerate perturbation theory (QDPT)⁵⁹. Here, the NEVPT2 correction is used to adjust the Born-Oppenheimer energy contributions of the diagonal QDPT matrix elements.

In numerical implementations, a mean-field approximation of the Breit-Pauli operator is suitable to describe the second-order spin-orbit coupling (SOC) operator in case of lighter elements.⁶⁰ With the spin-sublevel dependent SOC matrix elements at hand, the QDPT matrix is diagonalized, yielding spin-coupled states as eigenvectors and the respective energy levels as eigenvalues. Then, the SOC contribution to the zero-field splitting (ZFS) parameters is extracted as the energy differences. Additionally, the spin-spin coupling (SSC) generated by the dipolar spin-spin interaction is added to the mean-field SSC operator to account for its contribution to ZFS. Note that the inclusion of SSC does not introduce new states, but rather modifies the energy levels of the obtained QDPT eigenstates.

III. TECHNICAL DETAILS OF THE CALCULATIONS

In this study, we applied the quantum chemical program package ORCA⁶¹ (version 5.0.3) for all computations. The samples of ORCA input files can be found in the Supporting Information.

For all MODELS, the geometry of all six relevant electronic states were optimized at state-specific CASSCF(6e,4o)/cc-pVDZ level, by following the gradients of the root of interest. At the resulting equilibrium geometries, numerical vibrational analyses (CASSCF(6e,4o)/cc-pVDZ) and single-point energy calculations (CASSCF(6e,4o)-NEVPT2/cc-pVDZ) were performed.

Calculations at the CASSCF level were performed assuming C_{1h} point group as it is applicable for both Jahn-Teller stable and Jahn-Teller distorted structures. Additionally, E_x and E_y states can be conveniently distinguished according to their irreducible representations (A' and A'' , respectively), which is mandatory for state-specific geometry optimizations. In case when state-specific features such as geometry relaxation were investigated, the weight of the root of interest was set to 100%, while other roots were kept at 0% (meaning their wavefunctions were computed but they did not contribute to orbital optimization). On the other hand, when properties involving multiple states (e.g. transition matrix elements) were calculated, the six roots were weighed evenly. Vibrational analysis performed at the CASSCF level of theory was carried out using numerical gradients without symmetry considerations as available in ORCA.

The CASSCF-NEVPT2 framework was tested on smaller cluster models using both the strongly contracted and the fully internally contracted implementation of the ORCA suit, yielding a spectrum with tolerable discrepancy. The results discussed in the main text were obtained using the fully internally contracted approach.

All presented results were obtained in cc-pVDZ basis⁶². Note that, according to our preliminary analysis performed using cc-pVDZ, cc-pVTZ and cc-pVQZ basis sets⁶², only the spectrum of MODEL-1, see Fig. 1 was found to be slightly susceptible to the choice of basis, while larger clusters were insensitive up to 0.05 eV in average.

To speed up calculations, we took advantage of the resolution of identity approximation (RI). The construction of Coulomb- and exchange integrals was carried out in the RIJCOSX framework with def2/J auxiliary basis set. In the RI-NEVPT2 calculations, cc-pVDZ/C auxiliary basis set was applied. Note that RI-NEVPT2 implementation of ORCA does not benefit from symmetry. Nevertheless, the symmetry-adapted CASSCF orbitals were used as input.

The main text focuses solely on the results obtained with MODEL-3. The complete numerical analysis was also performed for MODEL-1 and 2, confirming the rapid convergence of our cluster models with respect to the size

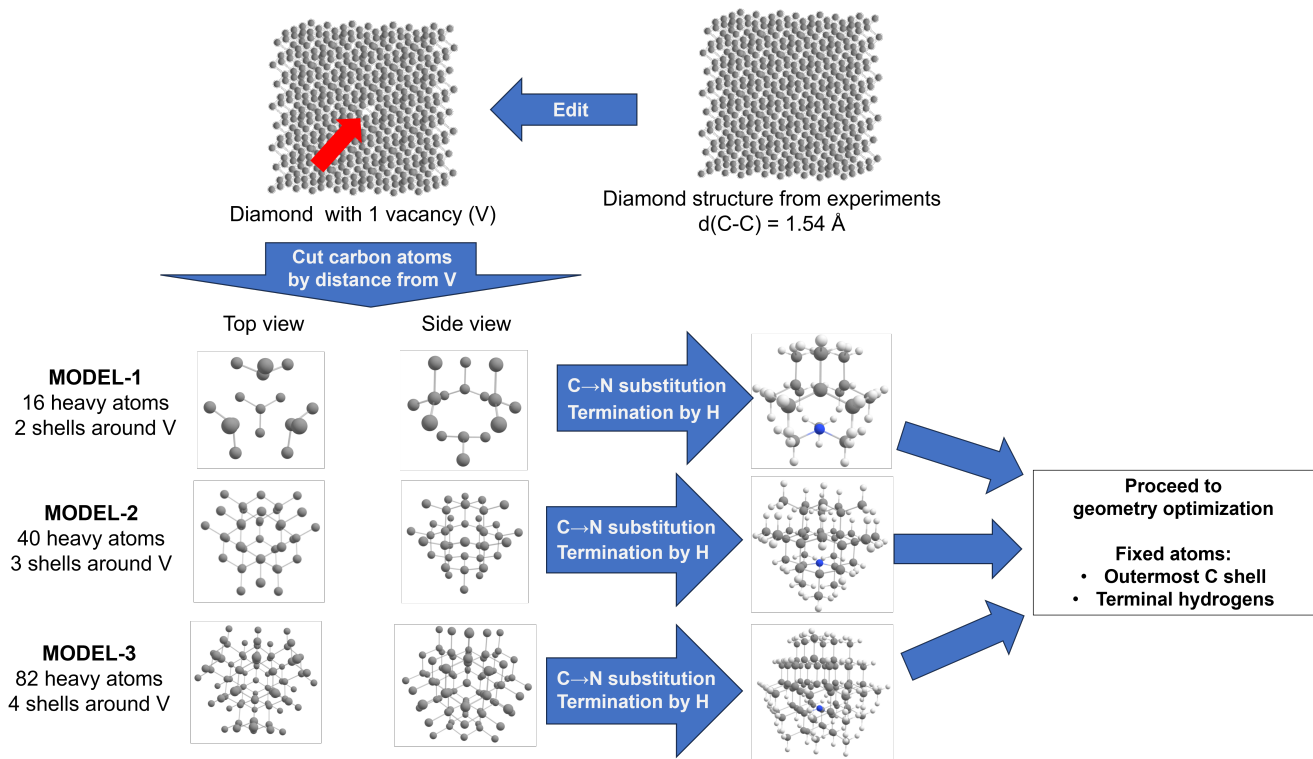


FIG. 1. Construction of the studied molecular models of the NV center.

of nanodiamond.

IV. OPTIMIZATION OF CLUSTER MODELS

The NV defect in diamond comprises a substitutional nitrogen atom paired with an adjacent vacancy. In its negative charge state, it manifests a triplet ground state characterized by C_{3v} symmetry.¹¹ In our molecular investigation, we employ quantum chemical models to simulate NV center embedded within nanodiamonds terminated with hydrogen at the surface. By progressively scaling up the cluster size, our objective is to accurately replicate the essential characteristics of the defected bulk crystal.

Large-scale bulk calculations, e.g., Ref. 63, indicate clearly that the defect center perturbs the perfect diamond crystal structure only in its close vicinity. Thus, to reflect the observed stiffness of the surrounding solid in our cluster models, we optimized atomic positions only near the vacancy while enforcing the perfect diamond structure in the outer shells of the cluster.

In the following, we discuss this scheme, depicted in Fig. 1, in more details. Initially, a sizeable pristine diamond of cubic crystal structure was formed with C-C bond distances, corresponding to the experimentally measured value of 1.54 Å. After removing a carbon atom

close to the center of this structure, the remaining carbons were divided into "shells" according to their position relative to the vacancy: atoms at n chemical bonds distance were assigned to the n th shell. Note that the first and second shells contain 4 and 12 carbons, respectively. In our most compact defected cluster model, denoted as MODEL-1, we consider a structure where one C atom of the first shell is substituted by nitrogen and the surface were capped by hydrogens in the following manner. Each carbon atom of the adjacent third shell were replaced by either 1, 2, or 3 hydrogens to saturate all dangling bonds of the second shell of the model. Motivated by hybrid theories⁶⁴ and by preserving the diamond crystal structure, we opt to adjust the length of these single C-H bonds to the conventional value of 1.09 Å without altering the positions of the hydrogens any further. During the geometry optimization process, the position of the terminating hydrogens and the carbons in the outermost shell are kept fixed, while allowing relaxation only for the atoms in the inner shells.

Note that this approach requires at least 2 shells around the vacancy; hence, MODEL-1 is the minimal conceivable size. Larger clusters, MODEL-2 and MODEL-3, were constructed analogously considering models of carbons up to the third and fourth shell, respectively.

By constraining the position of the outer atoms, our

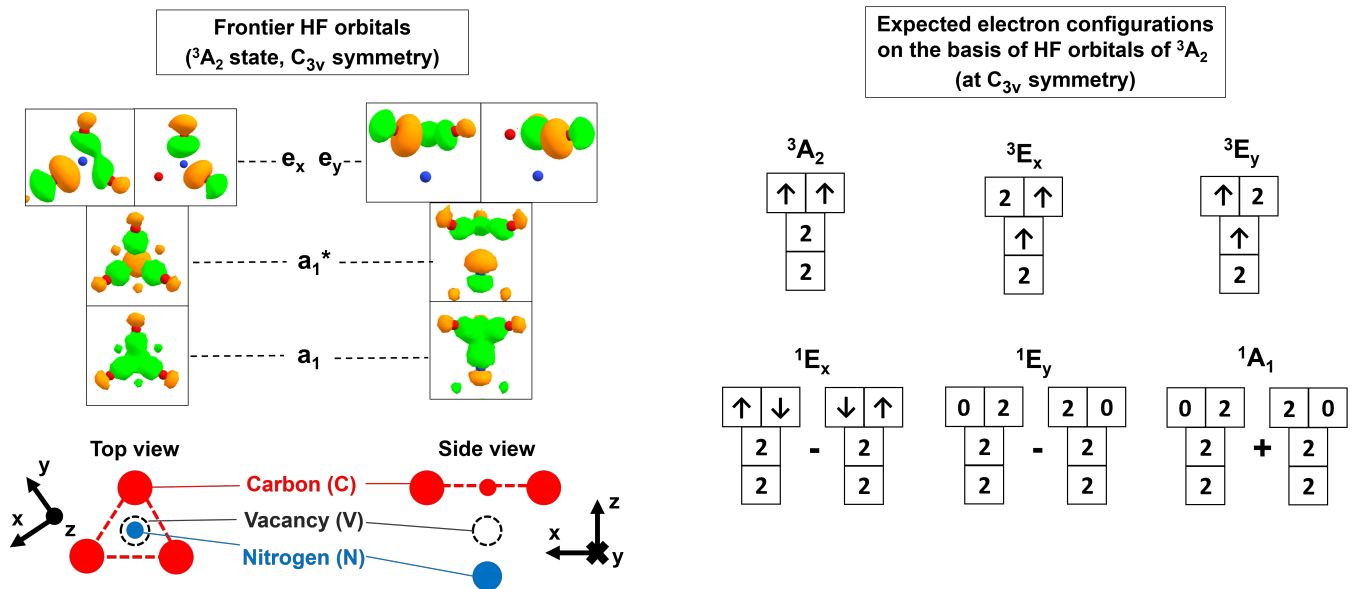


FIG. 2. Left: shape of the frontier Hartree–Fock molecular orbitals which form the active space for CASSCF(6e,4o) calculations. Right: Expected dominant electron configurations of NV⁻ electronic states involved in the spin polarization loop.

model not only considers the compression of the bulk material, but also the relatively limited number of atoms to be relaxed, giving the chance to perform geometry optimization on a high-level theory for all states of interest. While the accurate modeling of transition energies requires the comprehensive treatment of correlation effects, the geometry optimization, which involves bond stretching processes, can be readily performed by capturing merely the static correlations. Therefore, we applied the CASSCF approach for the constrained relaxation of the cluster models. These calculations were feasible in practice since in MODEL-1, 2, and 3 one only has to optimize the position of 4, 16, and 40 atoms, respectively.

V. RESULTS AND DISCUSSION

A. Defect orbitals

We begin our investigation by examining the Hartree–Fock orbitals of the defective nanodiamond, computed for the 3A_2 ground state. The four defect orbitals of sp^3 hybrid character situated within the band gap of the nanodiamond are illustrated in Fig. 2 (left). These orbitals correspond to the dangling bonds of the three carbons and the nitrogen adjacent to the vacancy. Among these, the a_1 is a bonding orbital shared between the three carbon and nitrogen atoms, while a_1^* is its antibonding pair. The degenerate orbitals e_x and e_y , which are responsible for the spin-density distribution, are localised exclusively on the carbon atoms.

Collectively, these four in-gap orbitals are occupied by six valence electrons, the distribution of which is ex-

pected to characterize the low-energy spectrum⁶⁵. More specifically, the spin-polarization loop of NV⁻ progresses through the six lowest-lying singlet and triplet electronic states, i.e., 3A_2 , 1A_1 , and the doubly degenerate 3E , 1E states.⁶⁶ The dominant electron configurations of these states, determined through group theoretical considerations⁶⁵, are presented on the right part of Fig. 2. While single-reference methods can approximate these many-body states to a certain extent, state mixing in the singlets can become crucial, a complexity addressed by the CASSCF method in our computational model.

B. Vertical electronic spectrum

Furthermore, we used the natural orbitals from the state-averaged CASSCF(6e,4o)/cc-pVDZ solution obtained at the ground state geometry to study the composition of the electronic states. As shown in Fig. 3, the triplet states are clearly single-reference, meaning they can be effectively described by a single electron configuration. On the other hand, the singlet states show evidence of state-mixing in line with our expectations. Specifically, the 1A_1 CASSCF eigenstate contains not only the dominant configurations proposed by group theory (76%) but also the configuration with an empty a_1^* orbital (24%). The 1E CASSCF eigenstates admixes the spin-singlet counterpart of the 3E states (18%) to the group-theoretic states (82%). Note that the observed state mixing, especially for 1A_1 , cannot be treated by conventional DFT based methods.

Now, we turn the focus to the discussion of the excitation energies, see Fig. 3. Analyzing the numerical data,

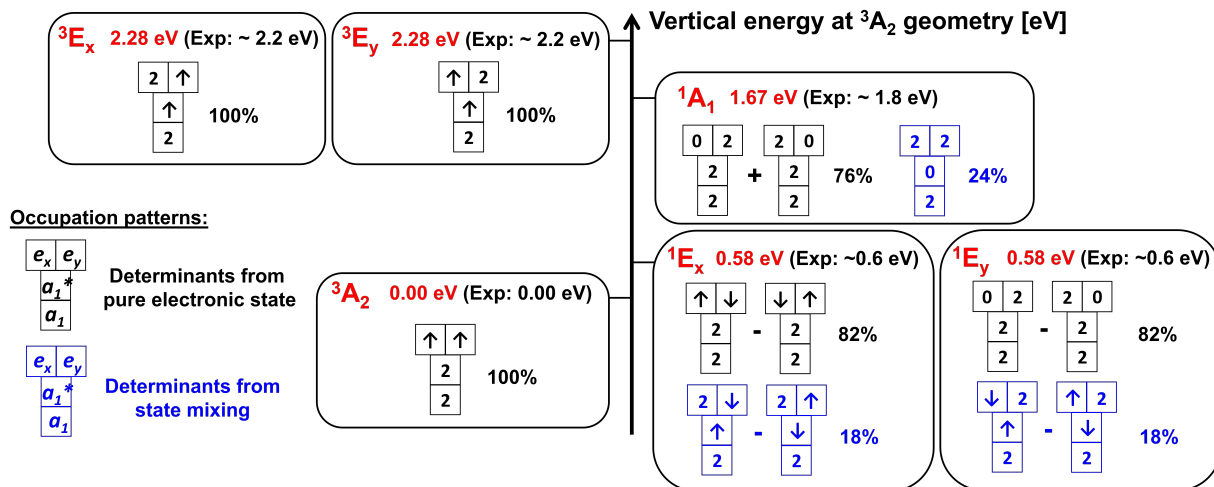


FIG. 3. Composition of electronic states at 3A_2 geometry, expressed in the basis of SA-CASSCF natural orbitals. Vertical excitation energies (CASSCF(6e,4o)-NEVPT2/cc-pVDZ). Accurate experimental data is available for the vertical singlet and triplet optical transitions 1.26⁶⁷ and 2.18⁶⁸ eV respectively. The energy shift of the singlet spectrum relative to ground state can be estimated²⁹ using the experimentally predicted ${}^3E^{-1}A_1$ adiabatic gap which was found in the range of 0.32-0.41 eV⁶⁹⁻⁷¹. Note that the ${}^3E^{-1}A_1$ transition is not directly observable in experiments, which can lead to an uncertainty in the respective experimental value.

we observed that the application of the NEVPT2 correction on top of the CASSCF theory had a large impact by reducing the raw CASSCF gaps by 0.2-0.7 eV. In fact, the resulted CASSCF-NEVPT2 optical transitions are in great agreement with the experimental data deviating by only ~ 0.1 eV. Specifically, we predict 2.28 and 1.19 eV for the vertical triplet and singlet optical gaps while experiments provided 2.18 and 1.26 eV energies, respectively. From our vertical calculation, we deduce 0.61 eV for the ${}^3E^{-1}A_1$ energy gap which is comparable to the indirectly obtained adiabatic experimental findings of 0.32-0.41 eV.

C. Relaxed electronic spectrum

To determine adiabatic energy differences between the states that correspond to the experimental zero-phonon lines we optimized the geometry of each state using the state-specific CASSCF(6e,4o)/cc-pVDZ method. The accurate electronic energies were computed at CASSCF(6e,4o)-NEVPT2/cc-pVDZ level of theory while the zero point energy (ZPE) corrections were obtained using CASSCF(6e,4o)/cc-pVDZ.

The relaxed geometries and the excitation energies are summarized in Fig. 4. We find that 1A_1 conserves the C_{3v} symmetry of the 3A_2 ground state while the C-C distances are stretched to 2.70 Å. However, for the E states JT distortion is observed lowering the symmetry to C_{1h} and forming A' and A'' states. In the former case, one inner C-C distance elongates relative to the other two, but the system remains close to C_{3v} symmetry - only 0.02-0.04 Å deviations were observed. In the latter case, elongation occurs, and the two longer C-C distances exceed

the short C-C side by 0.09-0.14 Å. The more apparent symmetry breaking of A'' , as well as the orbital picture (Fig. 2), suggest that the $E_x \rightarrow A''$ configuration is the more stable JT state; namely, the e_x orbital, which has bonding character is more populated in these structures than the antibonding e_y .

Nevertheless, the energy difference between A' and A'' states, which is in the range of ten of *milli* eVs, cannot be reliably predicted by CASSCF-NEVPT2 - partly because this small difference lies within the error margin of NEVPT2, and partly due to the fact that the optimization was carried out at CASSCF (rather than CASSCF-NEVPT2) level. Thus, the order of JT states in Fig. 4 reflects mere chemical intuition at this point, and an average energy level is provided for the E states. A more sophisticated discussion of JT energy levels can be found in the next section.

Studying the adiabatic spectrum of the color center depicted in Fig. 4, we found that the CASSCF-NEVPT2 excitation energies are close to the available experimental values with a deviation of less than 0.1 eV. In particular, for the transitions ${}^3E^{-3}A_1$, ${}^1E^{-1}A_1$ and ${}^3E^{-1}A_1$ our model neglecting the JT effects predicts 1.90, 1.10 and 0.30 eV which compares excellently to the adiabatic experimental data 1.95, 1.19 and 0.32-0.41 eV respectively.

D. Jahn-Teller behavior of E states

When studying the Jahn-Teller distorted 3E and 1E states, it is of fundamental interest whether the system is trapped in a single potential energy valley corresponding to an A'' structure (static Jahn-Teller effect), or con-

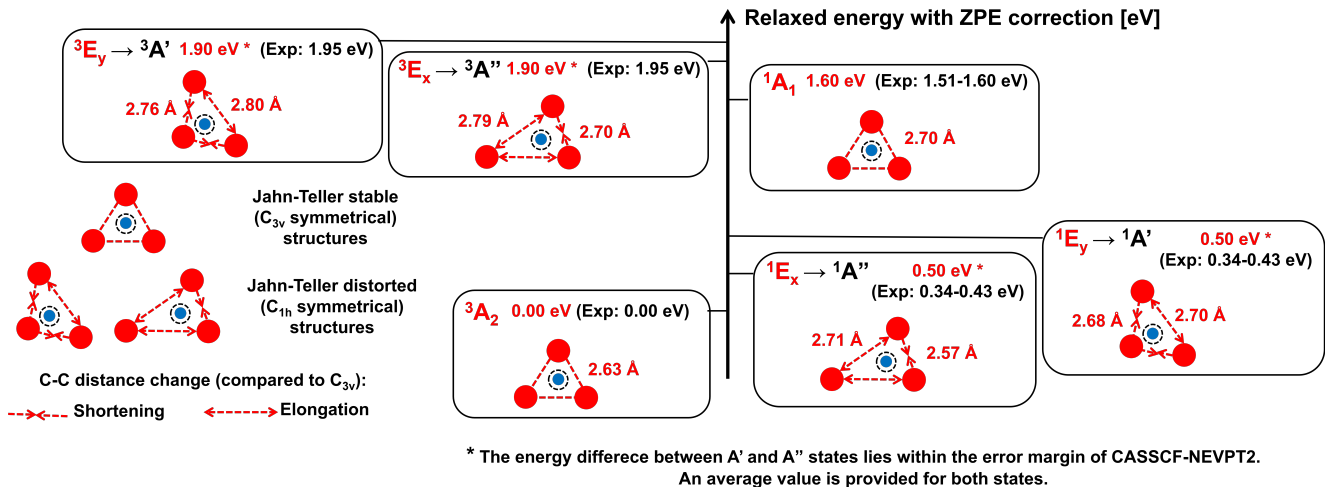


FIG. 4. Relaxed geometries (CASSCF(6e,4o)/cc-pVDZ), relaxed excitation energies (CASSCF(6e,4o)-NEVPT2/cc-pVDZ) with ZPE correction at CASSCF(6e,4o)/cc-pVDZ level. The complementing experimental data for the adiabatic singlet, triplet optical and ${}^3E \rightarrow {}^1A_1$ transitions is 1.19⁷², 1.95⁶⁸ and 0.32-0.41 eV⁶⁹⁻⁷¹ eV respectively. The overall energy spectrum was constructed as given in Ref. 29.

tinuously oscillates among three spatially degenerate A'' minima (dynamic Jahn-Teller effect). Namely, in the latter case, the system appears to be of high (C_{3v}) symmetry in experiments, even if the energetically most favorable geometry is distorted.

Static and dynamic Jahn-Teller systems can be distinguished by comparing the Jahn-Teller barrier (δ_{JT}) to the zero-point energy level of the two distortion-driving e vibrational modes ($h\nu_e$). Here, δ_{JT} refers to the energy difference between the two C_{1h} symmetrical configurations, i.e. A'' and A' (the latter acts as a transition state in Jahn-Teller oscillation). The criterion for a static JT effect is $\delta_{JT} > h\nu_e$; in the opposite case, the energy of the vibration is sufficiently large to form a dynamic JT system.⁷³

As visualized in Figure 5, δ_{JT} can be calculated at as an energy difference A'' and A' geometries. For this calculation, owing to the expected extremely small gap between the two equilibrium geometries, we used the level of geometry optimization. Namely, the SS-CASSCF potential energy surface is expected to be accurate in the vicinity of the equilibrium geometry, given that a single electronic state is studied. (A NEVPT2 correction would be disadvantageous for this calculation as the geometries were not optimized at NEVPT2 level. This discrepancy is negligible if energy differences of ≈ 1 eV size are studied, but causes large errors in the order of magnitude of meVs.

The Jahn-Teller barrier δ_{JT} was determined indirectly, as follows. In the first step, we searched for the minimum-energy crossing point (MECP) between E states by setting the weight of both E_x and E_y to 50% in the CASSCF optimization run. The resulting MECP (geometry for 3E and 1E is depicted in Fig. 5, see black frames) is the

most stable geometry where the E_x and E_y are degenerate, which is only possible at C_{3v} symmetry. Importantly, MECP can be considered as a part of both potential energy surfaces. As indicated in Fig. 5, the energy difference between MECP and the bottom of the A'' valley corresponds to the Jahn-Teller stabilization energy (E_{JT}), the role of which in the modeling is discussed below.

To gain accurate energy differences, we re-calculated the energy of MECP in SS-CASSCF calculations, setting the weight of E_x or E_y to 100%. These SS-CASSCF calculations target the same energy level in theory, but the result depends on the selected electronic state due to the slight alteration of active-space orbital shapes. Then, these energies can be directly compared to the SS-CASSCF energies for A'' and A' , which were obtained at the end of the geometry optimization run. E_{JT} can be calculated as the energy difference between MECP and A'' (using state-specific orbitals optimized for E_x); the difference between MECP and A' gives $E_{JT} - \delta_{JT}$ (using state-specific orbitals optimized for E_y); finally, δ_{JT} arises as the difference between the latter two amounts.

In the end, we obtained $\delta_{JT} = 26$ and 41 meV for 3E and 1E , respectively. To determine the nature of the JT effect, we first assumed static JT where A'' vibrates in its own potential valley. The vibrational analysis on this geometry resulted in $h\nu_e$ values of 84-88 meV for ${}^3A''$ and 75-80 meV for ${}^1A''$ (the degeneracy of e phonons is broken due to the decreased symmetry in A''). This, however, clearly contradicts the initial assumption - the system has enough vibrational energy, even at 0 K, to cross the barrier. Therefore, both 3E and 1E will be handled as dynamic JT systems in the following.

In dynamic JT, the strength of the vibronic coupling, i.e. the proportion of the Jahn-Teller stabilization energy

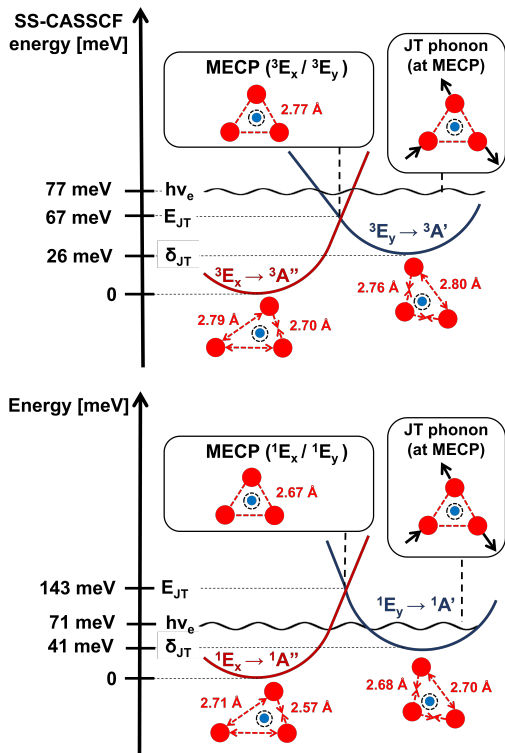


FIG. 5. Schematic representation of potential energy hyper-surfaces in the vicinity of the minimum-energy crossing points (MECPs) between 3E states (up) and 1E states (down). The relative energy levels of A' , A'' and MECP structures were calculated at the level of geometry optimization, i.e. state-specific CASSCF(6e,4o). Jahn-Teller parameters (E_{JT} , δ_{JT}) were obtained from SS-CASSCF energy differences, as shown, while the energy of the Jahn-Teller phonon ($h\nu_e$) was derived from the vibrational analysis of the MECP geometry, setting 50-50% weight for the two degenerate E states.

(E_{JT}) and the Jahn-Teller phonon energy ($h\nu_e$) characterizes the behavior of the system; it determines how the observed properties, such as the fine structure (*vide infra*) is altered compared to the Born-Oppenheimer picture.

E_{JT} refers to the energy which is released upon symmetry breaking ($C_{3v} \rightarrow C_{1h}$). As it has been mentioned above, it equals to the energy difference between MECP and A'' . At SS-CASSCF level, we found $E_{JT} = 67$ and 143 meV for 3E and 1E , respectively.

$h\nu_e$ for the dynamic system was obtained from a vibrational analysis at MECP. (We recall that 50-50% weighing was used in CASSCF, under the condition of which MECP represents a minimum on PES. The actual JT surface is not differentiable at MECP.) The calculated zero-point JT vibrational energies are 67 and 71 meV for for 3E and 1E , respectively, as shown in Fig. 5 (black wavy lines).

Putting these data together, both systems turn out to be strongly coupled, as $h\nu_e$ and E_{JT} are commensu-

table. In the case of 3E , where E_{JT} is below $h\nu_e$, the C_{3v} symmetrical MECP is expected to serve as a reasonable molecular model for calculating properties. For 1E , on the other hand, stronger vibronic coupling is expected and computational results from MECP are less relevant.

E. Fine structure of triplet states

By applying quasi-degenerate perturbation theory on the six obtained CASSCF(6,4)/cc-pVDZ eigenstates, we computed the fine-structure splitting of the spin-triplet states. The data discussed below were calculated at the ground state (3A_2) equilibrium geometry, and the MECP geometry between 3E_x and 3E_y in the case of 3E .

The D tensor of the 3A_2 state was obtained as the energy difference between the ground QDPT state (corresponding to 3A_2 , $m_S = 0$) and the two lowest excited states (3A_2 , $m_S \pm 1$). We note that spin-spin coupling (SSC) effects dominate in ground-state zero-field splitting - QDPT with only SOC results in three degenerate sublevels for 3A_2 . As shown in the top row of Table I, a near-exact reproduction of experimental data (D = 3.10 GHz vs the measured D = 2.88 GHz) was achieved.

Next, we investigated the fine structure of the 3E electronic states. In the C_{3v} symmetry of the MECP geometry, two orbitally degenerate states are split into six spin sublevels by SOC and SSC, the relative energy levels of which can be characterized by three parameters: λ_z , D_{es} and Δ , see Fig. 6 for visual explanation. The modeling of this splitting is, however, more complicated than simply extracting the raw QDPT energies - some manual processing was required, as described below.

Firstly, as E_x and E_y electronic states are not entirely degenerate at the level of computation due to numerical noises, $\approx 0.002eV$ energy difference is observed at the C_{3v} symmetrical MECP geometry. Therefore, the electronic energy of the two 3E states of interest were manually adjusted to their average value before the ORCA QDPT treatment.

More importantly, the dynamic Jahn-Teller instability of the 3E states attenuates the bare λ_z and Δ splitting parameters obtained at MECP by the so-called Ham re-

TABLE I. Zero-field splitting parameters of triplet electronic states measured in GHz.

State	Parameter	Theory	Experiment
3A_2	D	3.10	2.88 ⁷⁴
3E	λ_z	24.7	-
	$p\lambda_z$	4.20	5.3 ⁷⁵
	D_{es}	2.17	1.42 ⁷⁵
	Δ	2.92	-
	$q\Delta$	1.71	1.55 ⁷⁵

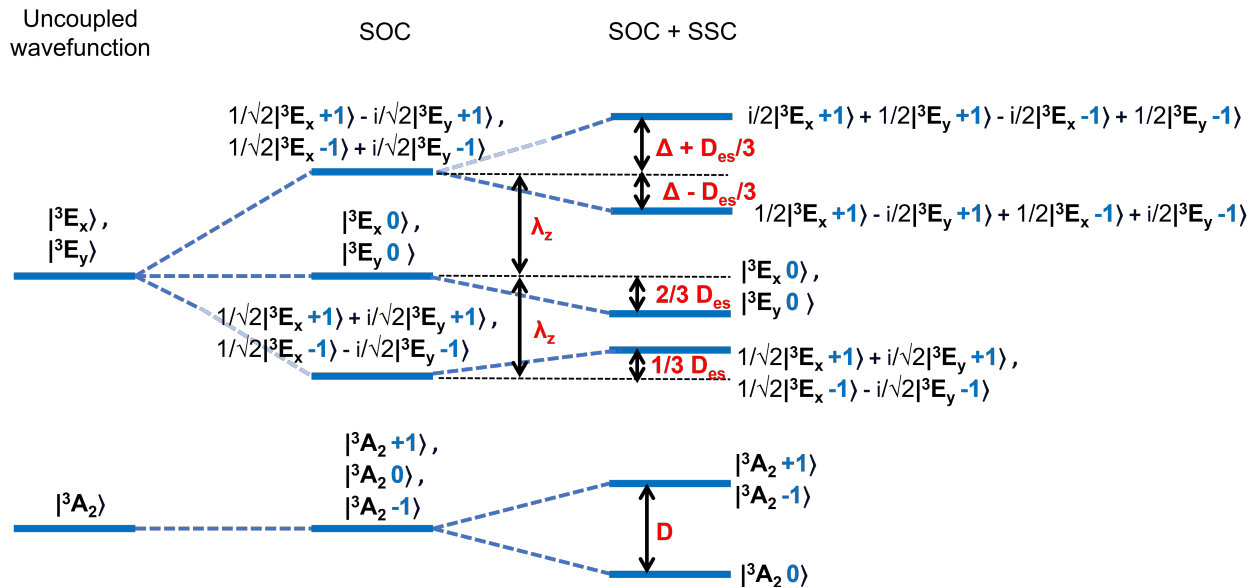


FIG. 6. Visualization of the definition of zero-field splitting parameters D , λ_z , D_{es} and Δ . The corresponding energy parameters are found in Tab. I. Some explanation: 3E_x , 3E_y : two degenerate 3E states (excitation to e_x or e_y orbital). Blue numbers - m_S quantum numbers. In the case of degenerate states, any linear combination can be an eigenfunction of the respective Hamiltonian.

duction factors⁷⁶. In our calculations, the corresponding multipliers were found to be $p=0.17$ and $q=0.59$.

Having the proper values at hand, the damped SOC elements $p\lambda_z$ and $q\Delta$ can be readily compared to the available experimental data as summarized in Table I. While raw λ_z is more than 5 times larger than the experimental value, the Ham-reduced result ($p\lambda_z = 4.20$ GHz) is in reasonable agreement with the measurements (5.3 GHz). Similarly, after taking into account the q reduction factor, the experimental Δ splitting of 1.55 GHz is reproduced by our calculations (1.71 GHz) with high accuracy. We note that the ab initio reproduction of these parameters is especially challenging due to the exponentialized $\frac{E_{JT}}{h\nu_e}$ term in the reduction factors, which easily introduces considerable errors. As for the D_{es} parameter, we obtained 2.17 GHz slightly overestimating the experimental 1.42 GHz.

In total, within the applied computational framework, experimental zero-field-splitting parameters were recovered with absolute errors of 0.1-1.1 GHz. The relative error are below 20%, with the sole exception of D_{es} , which is off by a factor of 1.5.

F. Spin-orbit coupling between singlet and triplet states

The probability of transition between singlet and triplet electronic states is determined in leading order by the corresponding spin-orbit coupling matrix element

(SOCME). We recall that SOCME is a three-dimensional vector, the square of which is directly proportional to the rate of transition according to Fermi's golden rule for intersystem crossing (ISC). Furthermore, the spin selectivity required for polarization and readout is also introduced to the theoretical modeling by SOCME, as ISC to/from the $m_s = 0$ sublevel of the triplet depends on its z -axis ("parallel") projection, while the other channel ($m_s = \pm 1$) is related to the xy -plane ("perpendicular") component. While the ab initio calculation of absolute transition rates by excited state dynamics is a complicated process and is out of the scope of this paper, the investigation of SOCMEs presented herein already provides some information about spin-polarization behavior of the system.

When calculating the SOCMEs, an important aspect is the choice of geometry. As the transition between electronic states occurs most likely in the vicinity of the minimum-energy crossing point (MECP) between the singlet and triplet potential energy surfaces, the MECP geometry would be the most rational choice. Nevertheless, MECP optimization is not as straightforward as the geometry optimizations for specific electronic states - for example, dynamic correlation is mandatory, in order to grasp the distance between the two crossing PESs correctly. As analytical gradients are usually not implemented for post-CASSCF methods in quantum chemical codes, MECP structures can only be obtained at large computational cost, which either derives from numerical gradient or a thorough potential energy surface scan.

TABLE II. Spin-orbit coupling matrix elements [GHz], calculated at the equilibrium geometry of the specified initial state. ΔE refers to the energy difference between states at initial-state geometry, which indicates the distance from the minimum-energy crossing point.

Transition	Initial state	Final state	ΔE [eV]	Channel	SOC matrix element	Experiment ⁷⁷
${}^3E \rightarrow {}^1A_1$	${}^3E_x \rightarrow {}^3A''$	1A_1	0.18	$m_s = \pm 1$	6.3 GHz	high selectivity (dominant: $m_s = \pm 1$)
	${}^3E_y \rightarrow {}^3A'$	1A_1		$m_s = 0$	5.1 GHz	
${}^1E \rightarrow {}^3A_2$	${}^1E_x \rightarrow {}^1A''$	3A_2	0.40	$m_s = \pm 1$	12.3 GHz	low selectivity (favored: $m_s = 0$)
	${}^1E_y \rightarrow {}^1A'$	3A_2		$m_s = 0$	0.0 GHz	
			0.43	$m_s = \pm 1$	14.1 GHz	
				$m_s = 0$	7.5 GHz	

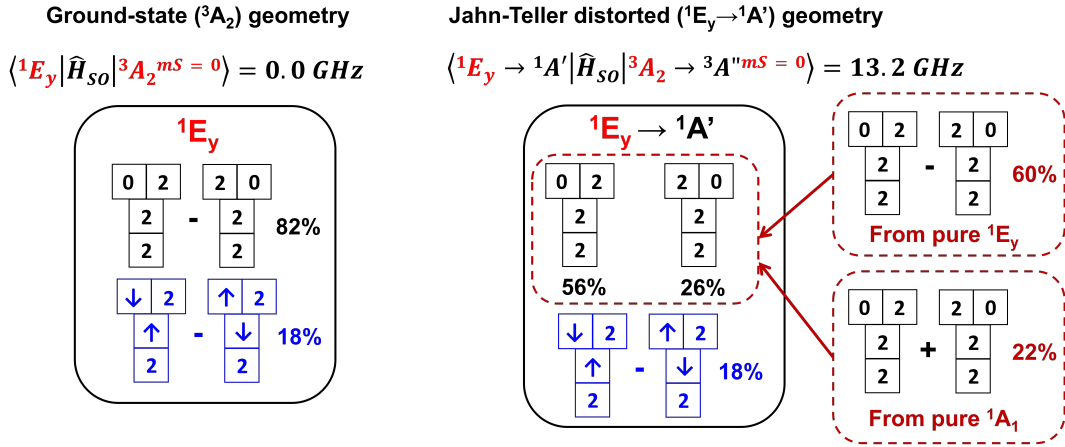


FIG. 7. CASSCF wavefunctions of the 1E_y electronic state, on the basis of SA-CASSCF natural orbitals. Left: At ground-state geometry, where no spin-orbit coupling is observed with 3A_2 at $m_s = 0$ channel. Right: At the Jahn-Teller distorted optimized geometry, where the two determinants of pure 1E_y are no longer equal in weight. This can be understood as a state mixing between 1E_y and 1A_1 , which induces significant spin-orbit coupling.

Herein, we present an initial investigation, where we assume that the equilibrium geometry of the initial, higher-energy state is reasonably close to MECP. In the ISC processes of the polarization cycle of NV⁻, where the energy gap between the electronic states involved in ISC is already small (${}^3E \rightarrow {}^1A_1 \approx 0.3 \text{ eV}$; ${}^1E \rightarrow {}^3A_2 \approx 0.5 \text{ eV}$), this is a reasonable starting point. Thus, SOCMEs at initial-state geometries will be discussed in the following.

Firstly, we examine the upper branch of the polarization cycle, i.e. the ${}^3E \rightarrow {}^1A_1$ transition (Tab. II, top row). As 3E is a DJT system, the coupling from both 3E_x and 3E_y (each at the respective Jahn-Teller distorted equilibrium geometry) is considered at state-average CASSCF(6e,4o) level. In both cases, we found significant ($\tilde{6}$ GHz) coupling to 1A_1 at the $m_s = \pm 1$ channel, while transition through $m_s = 0$ is only conceivable from ${}^3A''$ formed from 3E_y , and at a slightly lower strength of 5.4 GHz. These numbers are in agreement with experiments, which indicate that $m_s = 0$ is

the brighter state of NV⁻, and the intersystem crossing proceeds selectively through $m_s = \pm 1$. The energy difference between the initial and final states of ISC (3E and 1A_1) is 0.18 eV at initial-state geometry, which is commensurable to the error margin of NEVPT2. Therefore, these results closely represent the behavior at MECP, i.e. the actual geometry of transition where the energy difference (ΔE) is zero.

Next, we moved on to the lower branch, where the ${}^1E \rightarrow {}^3A_2$ transition closes the polarization cycle (Tab. II, top row). Conspicuously, the selectivity of A' and A'' states is reversed compared to the case of 3E : ${}^1E_x \rightarrow {}^1A''$ is a highly spin-selective process, clearly favoring $m_s = \pm 1$ (SOCME = 12.3 GHz), while 1E_y couples to ${}^1A''$ at both channels. The underlying reason is that the ground state has A'' irreducible representation in C_{1h} symmetry (in contrast to 1A_1 , which turns to A'), as a result of which the selection rules are reversed. Even though the $m_s = 0$ channel, which is required for closing the polar-

ization circle, is not favored even from the JT-distorted 1E_y (SOCME = 7.5 GHz vs 14.1 GHz for 0 and ± 1 sub-levels, respectively), this does not necessarily mean that our calculations are inaccurate. The relatively high gap of $\tilde{0.4}$ eV between 1E_y and 3A_2 at the geometry of the former strongly suggests that we are far from the more relevant MECP structure. Thus, MECP optimization, which is a subject of our ongoing research, seems crucial to characterize the lower branch of the nonradiative pathway.

It is interesting to analyze why the $m_s = 0$ channel is only accessible through one of the E states. We illustrate the electronic structure related reasons on the example of 1E_y , the wavefunction of which is provided in Fig. 7. (For the sake of clarity and consistency, we use SA-CASSCF wavefunctions and natural orbitals in this representation.) At C_{3v} symmetrical geometry (left side of the Figure), the determinants of the pure 1E_y state (black color) do not provide any coupling to 3A_2 , and even the determinants from state mixing (blue) interact only through $m_s = \pm 1$. On the other hand, after symmetry breaking by Jahn-Teller distortion (right side), the weight of closed-shell determinants is no longer equal in the wave function, which can be grasped an additional state mixing between 1E_y and 1A_1 states (see red dashed frames), both of which possess A' irreducible representation at C_{1h} symmetry. It is this particular mixing (also termed as pseudo-Jahn-Teller effect in the literature⁷⁸ that makes the transition through $m_s = 0$ feasible. Importantly, E_x has a different representation (A'') even at reduced symmetry, the coupling between E_x and 1A_1 remains zero, regardless of the geometry.

Altogether, as our wave-function based methodology takes all SOC-inducing state mixing effects by construction, the calculated spin selectivity of ISC processes matches the expectations from experiments. Future work will focus on the ab initio computation of absolute ISC (and photoluminescence) rates.

VI. CONCLUSION

In this theoretical study, we aimed to devise a wave-function only computational protocol which enables the full characterization of future quantum bit candidates implemented by point defects in semiconductors. The

proposed methodology was tested on the notorious NV⁻ center in diamond, by reproducing the available experimental data with tolerable error margins.

Our molecular-cluster based framework accounts for static electron correlation at CASSCF level, placing the chemically relevant defect orbitals to the active space. Dynamic correlation of the environment was computed at NEVPT2 level which provides a perturbative correction. The cluster geometries were optimized on CASSCF level of theory considering the stiffness of the hosting crystal.

We expect that the presented modeling approach can be routinely applied with similar accuracy for color centers in covalent crystals featuring up to 6-10 active defect orbitals.

ACKNOWLEDGMENTS

We acknowledge fruitful discussions with Rohit Babar, Gergő Thiering, Ádám Gali and Michael Roemelt. Helpful computational tweaks learned from the community of the ORCA Forum are also greatly appreciated.

This research was supported by the National Research, Development, and Innovation Office of Hungary within the Quantum Information National Laboratory of Hungary (Grant No. 2022-2.1.1-NL-2022-00004) and within grants FK 135496 and FK 145395. V.I. also acknowledges the support from the Knut and Alice Wallenberg Foundation through WBSQD2 project (Grant No. 2018.0071). A.P. acknowledges the financial support of János Bolyai Research Fellowship of the Hungarian Academy of Sciences.

The computations were enabled by resources provided by the National Academic Infrastructure for Supercomputing in Sweden (NAISS) and the Swedish National Infrastructure for Computing (SNIC) at NSC, partially funded by the Swedish Research Council through grant agreements no. 2022-06725 and no. 2018-05973. We also acknowledge KIFÜ for awarding us computational resources at the Komondor supercomputer in Hungary.

REFERENCES

-
- * ivady.viktor@ttk.elte.hu
 - † barcza.gergely@wigner.hu
 - ¹ C. L. Degen, F. Reinhard, and P. Cappellaro, *Rev. Mod. Phys.* **89**, 035002 (2017).
 - ² N. Aslam, H. Zhou, E. K. Urbach, M. J. Turner, R. L. Walsworth, M. D. Lukin, and H. Park, *Nature Reviews Physics* **5**, 157 (2023).
 - ³ C. J. Chunnillall, I. P. Degiovanni, S. Kück, I. Müller, and A. G. Sinclair, *Optical Engineering* **53**, 081910 (2014).
 - ⁴ I. Aharonovich, D. Englund, and M. Toth, *Nature Photonics* **10**, 631 (2016).
 - ⁵ G. Zhang, Y. Cheng, J.-P. Chou, and A. Gali, *Applied Physics Reviews* **7**, 031308 (2020), https://pubs.aip.org/aip/apr/article-pdf/doi/10.1063/5.0006075/14576561/031308_1_online.pdf.
 - ⁶ A. Aspuru-Guzik and P. Walther, *Nature Physics* **8**, 285 (2012).
 - ⁷ H.-K. Lo, M. Curty, and K. Tamaki, *Nature Photonics* **8**,

- 595 (2014).
- ⁸ T. D. Ladd, F. Jelezko, R. Laflamme, Y. Nakamura, C. Monroe, and J. L. O'Brien, *Nature* **464**, 45 (2010).
 - ⁹ D. D. Awschalom, L. C. Bassett, A. S. Dzurak, E. L. Hu, and J. R. Petta, *Science* **339**, 1174 (2013).
 - ¹⁰ D. Suter, "Optical detection of magnetic resonance," (2020).
 - ¹¹ Ádám Gali, *Nanophotonics* **8**, 1907 (2019).
 - ¹² H. Ma, N. Sheng, M. Govoni, and G. Galli, *Journal of Chemical Theory and Computation* **17**, 2116 (2021), <https://doi.org/10.1021/acs.jctc.0c01258>.
 - ¹³ W. Pfäffle, D. Antonov, J. Wrachtrup, and G. Bester, *Phys. Rev. B* **104**, 104105 (2021).
 - ¹⁴ L. Muechler, D. I. Badrtdinov, A. Hampel, J. Cano, M. Rösner, and C. E. Dreyer, *Phys. Rev. B* **105**, 235104 (2022).
 - ¹⁵ R. O. Jones, *Rev. Mod. Phys.* **87**, 897 (2015).
 - ¹⁶ C. Freysoldt, B. Grabowski, T. Hickel, J. Neugebauer, G. Kresse, A. Janotti, and C. G. Van de Walle, *Rev. Mod. Phys.* **86**, 253 (2014).
 - ¹⁷ C. E. Dreyer, A. Alkauskas, J. L. Lyons, A. Janotti, and C. G. Van de Walle, *Annual Review of Materials Research* **48**, 1 (2018).
 - ¹⁸ A. J. Cohen, P. Mori-Sánchez, and W. Yang, *Chemical Reviews* **112**, 289 (2012), <https://doi.org/10.1021/cr200107z>.
 - ¹⁹ P. Verma and D. G. Truhlar, *Trends in Chemistry* **2**, 302 (2020), special Issue - Laying Groundwork for the Future.
 - ²⁰ P. Makkar and N. N. Ghosh, *RSC Adv.* **11**, 27897 (2021).
 - ²¹ M. W. Doherty, N. B. Manson, P. Delaney, F. Jelezko, J. Wrachtrup, and L. C. Hollenberg, *Physics Reports* **528**, 1 (2013), the nitrogen-vacancy colour centre in diamond.
 - ²² Ádám Gali, *Nanophotonics* **12**, 359 (2023).
 - ²³ K. Raghavachari, D. Ricci, and G. Pacchioni, *The Journal of Chemical Physics* **116**, 825 (2002), https://pubs.aip.org/aip/jcp/article-pdf/116/2/825/19324682/825_1_online.pdf.
 - ²⁴ A. Gali, *physica status solidi (b)* **248**, 1337 (2011), <https://onlinelibrary.wiley.com/doi/pdf/10.1002/pssb.201046254>.
 - ²⁵ Y. Jin, M. Govoni, and G. Galli, *npj Computational Materials* **8**, 238 (2022).
 - ²⁶ Y. Jin, V. W.-z. Yu, M. Govoni, A. C. Xu, and G. Galli, *Journal of Chemical Theory and Computation* **19**, 8689 (2023), <https://doi.org/10.1021/acs.jctc.3c00986>.
 - ²⁷ A. V. Ivanov, Y. L. A. Schmerwitz, G. Levi, and H. Jónsson, *SciPost Phys.* **15**, 009 (2023).
 - ²⁸ A. S. Zyubin, A. M. Mebel, M. Hayashi, H. C. Chang, and S. H. Lin, *Journal of Computational Chemistry* **30**, 119 (2009), <https://onlinelibrary.wiley.com/doi/pdf/10.1002/jcc.21042>.
 - ²⁹ C. Bhandari, A. L. Wysocki, S. E. Economou, P. Dev, and K. Park, *Phys. Rev. B* **103**, 014115 (2021).
 - ³⁰ P. Delaney, J. C. Greer, and J. A. Larsson, *Nano Letters* **10**, 610 (2010), <https://doi.org/10.1021/nl903646p>.
 - ³¹ M. Bockstedte, F. Schütz, T. Garratt, V. Ivády, and A. Gali, *npj Quantum Materials* **3**, 31 (2018).
 - ³² G. Barcza, V. Ivády, T. Szilvási, M. Vörös, L. Veis, A. Gali, and O. Legeza, *Journal of Chemical Theory and Computation* **17**, 1143 (2021).
 - ³³ M. Li, R. Kobayashi, R. D. Amos, M. J. Ford, and J. R. Reimers, *Chemical Science* **13**, 1492 (2022).
 - ³⁴ Y. Ma, M. Rohlfing, and A. Gali, *Phys. Rev. B* **81**, 041204 (2010).
 - ³⁵ S. Choi, M. Jain, and S. G. Louie, *Phys. Rev. B* **86**, 041202 (2012).
 - ³⁶ H. Ma, M. Govoni, and G. Galli, *npj Computational Materials* **6**, 85 (2020).
 - ³⁷ N. Sheng, C. Vorwerk, M. Govoni, and G. Galli, *Journal of Chemical Theory and Computation* **18**, 3512 (2022), pMID: 35648660, <https://doi.org/10.1021/acs.jctc.2c00240>.
 - ³⁸ Y. Chen, T. Jiang, H. Chen, E. Han, A. Alavi, K. Yu, E. Wang, and J. Chen, *Phys. Rev. B* **108**, 045111 (2023).
 - ³⁹ S. Haldar, A. Mitra, M. R. Hermes, and L. Gagliardi, *The Journal of Physical Chemistry Letters* **14**, 4273 (2023), pMID: 37126760, <https://doi.org/10.1021/acs.jpcllett.3c00551>.
 - ⁴⁰ P. Siegbahn, A. Heiberg, B. Roos, and B. Levy, *Physica Scripta* **21**, 323 (1980).
 - ⁴¹ B. O. Roos, P. R. Taylor, and P. E. Siegbahn, *Chemical Physics* **48**, 157 (1980).
 - ⁴² P. E. M. Siegbahn, J. Almlöf, A. Heiberg, and B. O. Roos, *The Journal of Chemical Physics* **74**, 2384 (1981), https://pubs.aip.org/aip/jcp/article-pdf/74/4/2384/18926917/2384_1_online.pdf.
 - ⁴³ Z. Tóth and P. Pulay, *Journal of Chemical Theory and Computation* **16**, 7328 (2020), <https://doi.org/10.1021/acs.jctc.0c00123>.
 - ⁴⁴ M. W. Doherty, N. B. Manson, P. Delaney, F. Jelezko, J. Wrachtrup, and L. C. Hollenberg, *Physics Reports* **528**, 1 (2013).
 - ⁴⁵ H. Stoll, *Phys. Rev. B* **46**, 6700 (1992).
 - ⁴⁶ G. H. Booth, A. Grüneis, G. Kresse, and A. Alavi, *Nature* **493**, 365 (2013).
 - ⁴⁷ J. McClain, Q. Sun, G. K.-L. Chan, and T. C. Berkelbach, *Journal of Chemical Theory and Computation* **13**, 1209 (2017), <https://doi.org/10.1021/acs.jctc.7b00049>.
 - ⁴⁸ R. Babar, G. Barcza, A. Pershin, H. Park, O. B. Lindvall, G. Thiering, O. Legeza, J. H. Warner, I. A. Abrikosov, A. Gali, and V. Ivády, *arXiv:2111.09589 [cond-mat]* (2021), 2111.09589.
 - ⁴⁹ Z. Benedek, R. Babar, Á. Ganyecz, T. Szilvási, Ö. Legeza, G. Barcza, and V. Ivády, *npj Computational Materials* **9**, 187 (2023).
 - ⁵⁰ C. Angeli, R. Cimiraglia, S. Evangelisti, T. Leininger, and J.-P. Malrieu, *The Journal of Chemical Physics* **114**, 10252 (2001).
 - ⁵¹ C. Angeli, R. Cimiraglia, and J.-P. Malrieu, *The Journal of Chemical Physics* **117**, 9138 (2002), <https://doi.org/10.1063/1.1515317>.
 - ⁵² C. Angeli, M. Pastore, and R. Cimiraglia, *Theoretical Chemistry Accounts* **117**, 743 (2007).
 - ⁵³ C. Møller and M. S. Plesset, *Phys. Rev.* **46**, 618 (1934).
 - ⁵⁴ K. G. Dyall, *The Journal of Chemical Physics* **102**, 4909 (1995), https://pubs.aip.org/aip/jcp/article-pdf/102/12/4909/19185508/4909_1_online.pdf.
 - ⁵⁵ Y. Guo, K. Sivalingam, and F. Neese, *The Journal of Chemical Physics* **154**, 214111 (2021), https://pubs.aip.org/aip/jcp/article-pdf/doi/10.1063/5.0051211/16673662/214111_1_online.pdf.
 - ⁵⁶ C. Kollmar, K. Sivalingam, Y. Guo, and F. Neese, *The Journal of Chemical Physics* **155**, 234104 (2021), https://pubs.aip.org/aip/jcp/article-pdf/doi/10.1063/5.0072129/16704053/234104_1_online.pdf.
 - ⁵⁷ Y. Guo, K. Sivalingam, E. F. Valeev, and F. Neese, *J. Chem. Phys.* **144**, 094111 (2016).
 - ⁵⁸ Y. Guo, F. Pavosevic, K. Sivalingam, U. Becker, E. Valeev,

- and F. Neese, *The Journal of Chemical Physics* **158** (2023), [10.1063/5.0144260](https://doi.org/10.1063/5.0144260).
- ⁵⁹ M. Roemelt, D. Maganas, S. DeBeer, and F. Neese, *The Journal of Chemical Physics* **138**, 204101 (2013), https://pubs.aip.org/aip/jcp/article-pdf/doi/10.1063/1.4804607/13280319/204101_1_online.pdf.
- ⁶⁰ F. Neese, *The Journal of Chemical Physics* **122**, 034107 (2005), https://pubs.aip.org/aip/jcp/article-pdf/doi/10.1063/1.1829047/10872245/034107_1_online.pdf.
- ⁶¹ F. Neese, *Wiley Interdisciplinary Reviews: Computational Molecular Science* **12**, e1606 (2022).
- ⁶² T. H. Dunning, *The Journal of Chemical Physics* **90**, 1007 (1989), <https://doi.org/10.1063/1.456153>.
- ⁶³ I. Takács and V. Ivády, “Accurate hyperfine tensors for solid state quantum applications: Case of the nv center in diamond,” (2024), [arXiv:2309.03983 \[quant-ph\]](https://arxiv.org/abs/2309.03983).
- ⁶⁴ S. Dapprich, I. Komáromi, K. Byun, K. Morokuma, and M. J. Frisch, *Journal of Molecular Structure: THEOCHEM* **461-462**, 1 (1999).
- ⁶⁵ J. R. Maze, A. Gali, E. Togan, Y. Chu, A. Trifonov, E. Kaxiras, and M. D. Lukin, *New Journal of Physics* **13**, 025025 (2011).
- ⁶⁶ G. m. H. Thiering and A. Gali, *Phys. Rev. B* **98**, 085207 (2018).
- ⁶⁷ P. Kehayias, M. W. Doherty, D. English, R. Fischer, A. Jarmola, K. Jensen, N. Leefer, P. Hemmer, N. B. Manson, and D. Budker, *Phys. Rev. B* **88**, 165202 (2013).
- ⁶⁸ G. Davies and M. F. Hamer, *Proceedings of the Royal Society of London. Series A* **348**, 285 (1976).
- ⁶⁹ M. L. Goldman, A. Sipahigil, M. W. Doherty, N. Y. Yao, S. D. Bennett, M. Markham, D. J. Twitchen, N. B. Manson, A. Kubanek, and M. D. Lukin, *Phys. Rev. Lett.* **114**, 145502 (2015).
- ⁷⁰ M. L. Goldman, M. W. Doherty, A. Sipahigil, N. Y. Yao, S. D. Bennett, N. B. Manson, A. Kubanek, and M. D. Lukin, *Phys. Rev. B* **91**, 165201 (2015).
- ⁷¹ M. L. Goldman, M. W. Doherty, A. Sipahigil, N. Y. Yao, S. D. Bennett, N. B. Manson, A. Kubanek, and M. D. Lukin, *Phys. Rev. B* **96**, 039905 (2017).
- ⁷² L. J. Rogers, S. Armstrong, M. J. Sellars, and N. B. Manson, *New Journal of Physics* **10**, 103024 (2008).
- ⁷³ I. Bersuker, *The Jahn-Teller Effect* (University of Texas, Austin, 2006).
- ⁷⁴ J. H. N. Loubser and J. A. van Wyk, *Reports on Progress in Physics* **41**, 1201 (1978).
- ⁷⁵ A. Batalov, V. Jacques, F. Kaiser, P. Siyushev, P. Neumann, L. J. Rogers, R. L. McMurry, N. B. Manson, F. Jelezko, and J. Wrachtrup, *Phys. Rev. Lett.* **102**, 195506 (2009).
- ⁷⁶ F. S. Ham, *Phys. Rev.* **166**, 307 (1968).
- ⁷⁷ L. Robledo, H. Bernien, T. van der Sar, and R. Hanson, *New Journal of Physics* **13**, 025013 (2011).
- ⁷⁸ I. B. Bersuker, *Chemical Reviews* **121**, 1463 (2021), <https://doi.org/10.1021/acs.chemrev.0c00718>.